Inorganic Chemistry

Article

pubs.acs.org/IC

Crystal Chemistry, Band Engineering, and Photocatalytic Activity of the $LiNb_3O_8$–$CuNb_3O_8$ Solid Solution

Prangya Parimita Sahoo and Paul A. Maggard*

Department of Chemistry, North Carolina State University, Raleigh, North Carolina 27695-8204, United States

Supporting Information

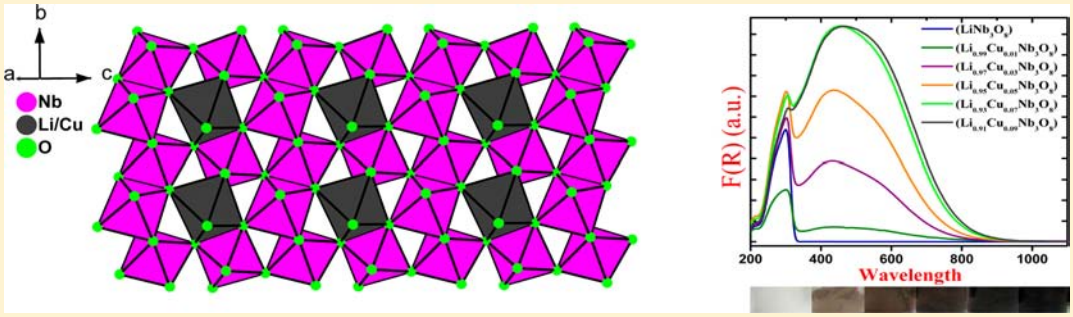

ABSTRACT: A new solid solution has been prepared in the system $LiNb_3O_8$–$CuNb_3O_8$, and the impacts of chemical composition and crystal structure have been investigated for the resulting band gap sizes and photocatalytic activities for water reduction to hydrogen under visible light. All members of the solid solution were synthesized by solid-state methods within evacuated fused-silica vessels, and their phase purities were confirmed via powder X-ray diffraction techniques (space group $P2_1/a$, a = 15.264(5)–15.367(1) Å, b = 5.031(3)–5.070(1) Å, c = 7.456(1)–7.536(8) Å, and β = 107.35(1)–107.14(8)°, for $0 \le x \le 1$). Rietveld refinements were carried out for the x = 0.09, 0.50, and 0.70 members of the solid solution, which reveal the prevailing isostructurality of the continuous solid solution. The structure consists of chains of $(Li/Cu)O_6$ and NbO_6 octahedra. The optical band gap size across the solid solution exhibits a significant red-shift from ~3.89 eV (direct) to ~1.45 eV and ~1.27 eV (direct and indirect) with increasing Cu(I) content, consistent with the change in sample color from white to dark brown to black. Electronic structure calculations based on density-functional theory methods reveal the rapid formation of a new Cu $3d^{10}$-based valence band that emerges higher in energy than the O 2p band. While the pure $LiNb_3O_8$ is a highly active UV-photocatalyst for water reduction, the $Li_{1-x}Cu_xNb_3O_8$ solid is shown to be photocatalytically active under visible-light irradiation for water reduction to hydrogen.

INTRODUCTION

The application of semiconductors as photocatalysts has drawn an increasing amount of recent research interest because of the potential to produce hydrogen as a renewable fuel source, using only sunlight and water.[1−7] Since the discovery of photocatalysis over TiO_2 by Fujishima and Honda, numerous catalysts have been investigated and found to be highly active under ultraviolet irradiation for the reduction of water to hydrogen, the oxidation of water to oxygen, or the overall splitting of water into both hydrogen and oxygen. However, as nearly one-half of the incident solar energy on the Earth's surface falls in the visible-light energy range, solid-state photocatalysts are sought that have band gap sizes that more closely match this lower-energy component of the solar spectrum. The synthesis of metal–oxide photocatalysts with visible-light band gap sizes can be realized using a couple of general strategies. One approach involves the substitution or doping of various nonoxide anions into their structures, such as in TiO_2, resulting in the photocatalysts such as $TiO_{2-x}N_x$ and $TiO_{2-x}C_x$.[8−10] Another main approach involves the synthesis of mixed-metal oxides that contain higher-energy valence bands based on filled metal-based orbitals, such as for $CaBi_2O_4$, Bi_2WO_6, $CaIn_2O_4$, $AgNbO_3$, and $AgGaO_2$.[11−17]

Band engineering has been a critical component, and is typically the first step in the preparation and identification of hitherto unexplored visible-light photocatalysts.[18] Examples from the literature have shown that $6s^2$ orbitals, for example, for Pb(II) and Bi(III), and $4d^{10}/3d^{10}$ orbitals, for example, for Ag(I) and Cu(I), can effectively create valence bands located higher in energy than that derived from the O 2p orbitals, and can thus shorten the energetic distance to the conduction band states.[12,19,20] Recently, our research efforts have targeted the preparation and investigation of new photocatalysts (in both polycrystalline film and powder forms) with small band gap sizes for metal oxides that combine Cu(I) (filled d^{10} orbitals) and Nb(V)/Ta(V) (empty d^0 orbitals) cations within their structures. This has resulted in the discovery of new p-type polycrystalline photoelectrodes that function for water reduction, including $CuNbO_3$, $CuNb_3O_8$, $Cu_5Ta_{11}O_{30}$, and

Received: December 3, 2012
Published: March 29, 2013

   dx.doi.org/10.1021/ic302649s | Inorg. Chem. 2013, 52, 4443−4450

$Cu_3Ta_7O_{19}$.[21−24] Several of these phases are also known to form solid solutions on the M(I) and M(V) cation sites such as in the new solid solution $(Na_{1-x})Cu_xTa_4O_{11}$ found in the $Na_2O-Cu_2O-Ta_2O_5$ system.[25] As a suspended metal−oxide powder in solution, these particles may be expected to exhibit photocatalytic activity at their surfaces, which has not previously been investigated.

Reported herein are the synthesis of members of a $LiNb_3O_8-CuNb_3O_8$ solid solution and an investigation of the effect of the Cu(I) content on the valence-band composition and energy, its electronic structure, and the photocatalytic activities of the particles in an aqueous solution. The solid solution reveals a dramatic red-shift of the band gap size upon the introduction of Cu(I) into this structure, which allows the investigation of the band gap sizes and photocatalytic activity across the solid solution. The products were characterized via Rietveld refinements of the powder X-ray diffraction data, as well as using UV−vis diffuse reflectance to determine the shifts in band gap sizes with composition. Insights into the origins of the band gap sizes were obtained from electronic structure calculations using density-functional theory methods.

EXPERIMENTAL SECTION

Materials and Synthesis. The reagents Li_2CO_3, Cu_2O, and Nb_2O_5 (Alfa Aesar, 99.99%) were used as received. First, $LiNbO_3$ was synthesized by heating Li_2CO_3 and Nb_2O_5 in open air at 900 °C for 6 h. Next, members of the solid solution $Li_{1-x}Cu_xNb_3O_8$ ($0 \le x \le 1$) were synthesized by the solid-state route by combining stoichiometric amounts of $LiNbO_3$, Cu_2O, and Nb_2O_5 loaded at the molar ratios appropriate for x = 0, 0.01, 0.03, 0.05, 0.07, 0.09, 0.1, 0.3, 0.5, 0.7, 0.9, and 1.0. The reactants were ground well in an agate mortar and pestle inside a glovebox, flame-sealed within evacuated fused-silica vessels, and fired at 750 °C for 48 h. All of the syntheses were carried out under vacuum. The color of the products varied from pristine white to dark brown to black with increase in Cu(I) content in the solid solution. The powder XRD patterns indicated the formation of single phases for the various compositions, Figure 1.

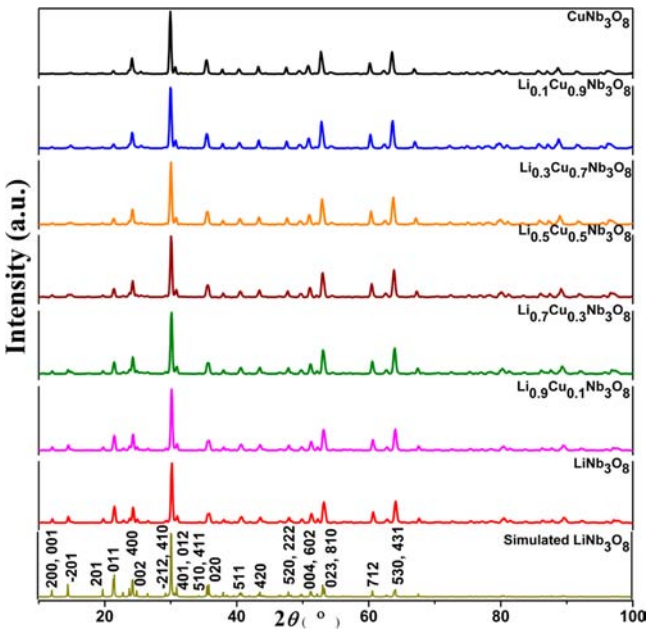

Figure 1. Powder XRD patterns of various members of the solid solution $Li_{1-x}Cu_xNb_3O_8$ ($0 \le x \le 1$). The simulated powder diffraction pattern of $LiNb_3O_8$ is given for comparison.

Characterization. Powder XRD data sets were collected for all samples at room temperature on a Rigaku R-Axis Spider with a curved image plate detector and Cu Kα radiation from a sealed-tube X-ray source over the angular range $10° \le 2\theta \le 100°$, with a step width of 0.01° at room temperature and calibrated against silicon powder (NIST-SRM 640c) standards. A Le Bail profile analysis in the JANA2000 suite was used to refine the X-ray diffraction data.[26] The background was estimated by a Legendre polynomial function consisting of 15 coefficients, and the peak shapes were described by a pseudo-Voigt function varying five profile coefficients. A scale factor, a zero error factor, and shape were refined. The 2θ range 14.5−15.6 was masked during the refinement, as the reflection at this range corresponded to the quartz capillary used for mounting the sample. Three members of the solid solution $Li_{1-x}Cu_xNb_3O_8$ ($0 \le x \le 1$), that is, for x = 0.09, 0.50, and 0.70, were selected for the collection of high-resolution Rietveld quality PXRD data at room temperature on a RIGAKU DMAX 2100 powder X-ray diffractometer using Cu Kα radiation. Diffraction data were collected in the 2θ range from $10° \le 2\theta \le 110°$ in step sizes of 0.017° with a scan speed of 0.149°/min. The data were analyzed by Le Bail profile analysis and then refined by the Rietveld method as implemented in the JANA2000 program suite. The asymmetry in the peak shape was treated by Berar−Baldinozzi function included in JANA2000. The positional and isotropic displacement parameters were also refined.

The UV−vis diffuse reflectance spectrum of each sample was collected on a Shimadzu spectrometer UV-3600 with the help of an integrating sphere in the wavelength range of 200−1300 nm. Approximately 20 mg of each sample was mounted onto a sample holder by pressing the powder into a $BaSO_4$ matrix and placing it along the external window of the integrating sphere. A sample of pure pressed barium sulfate powder was prepared as a reference, and the data were plotted as the function $F(R) = (1 - R_\infty)^2/(2R_\infty)$, where R is diffuse reflectance based on the Kubelka−Munk theory of diffuse reflectance.[27,28] The Tauc plot method is a widely accepted technique for determining the direct and indirect band gap sizes.[29] The absorption edge and the photon energy are related by the equation $(\alpha h\nu)^n = A(h\nu - E_g)$, where h is Planck's constant, ν is frequency, α is absorption coefficient, E_g is band gap size, and A is proportionality constant. The value of the exponent n denotes the nature of transition: 2 for direct allowed and 1/2 for indirect allowed. Thus, the band gap sizes can be extracted via Tauc plots of $[\alpha h\nu]^n$ versus $(h\nu)$. However, because α is proportional to $F(R)$, the Tauc equation can be expressed as a function of $F(R)$, and plots of $[F(R)h\nu]^n$ versus $h\nu$ can be used to extract the direct and indirect band gap sizes. The diffuse reflectance UV−vis data for analysis of the direct and indirect band gap sizes of individual members of the solid solution are provided in the Supporting Information.

Photocatalysis Measurements. The photocatalytic activity of each sample for the reduction of water to hydrogen was carried out using an outer-irradiation type fused-silica reaction cell with a volume of 90 mL and irradiated under visible light (λ > 420 nm). This procedure has been described previously,[19,20] and so is described briefly. First, each sample was loaded with a 1 wt % Pt cocatalyst using the photodeposition method.[30] Previous studies have shown that the loading of small amounts of Pt islands onto the metal−oxide surfaces increases the reaction rate through an enhanced separation of the photogenerated electrons and holes[31,32] as well as by decreasing the overpotential for hydrogen formation from water at the surface.[33,34] Typically, 100 mg of the sample was mixed with 30 mL of an aqueous solution of dihydrogen hexachloroplatinate(IV) ($H_2PtCl_6{\cdot}6H_2O$; Alfa Aesar, 99.95%), which was then irradiated for 2 h using a 400 W Xe arc-lamp with constant stirring using a magnetic stir bar. A few milliliters of methanol was added to each vessel before the reaction to assist in the Pt deposition. After platinization, the catalyst particles were separated via centrifugation, washed with deionized water several times to remove any remaining chloride ions, and then dried overnight in an oven at 80 °C. The platinized metal−oxide samples (100 mg) were next dispersed in a 20% aqueous methanol solution and stirred in the dark for ∼2 h, to remove the trapped gases on the particles' surfaces. The quartz reaction vessel was irradiated under constant

dx.doi.org/10.1021/ic302649s | Inorg. Chem. 2013, 52, 4443−4450

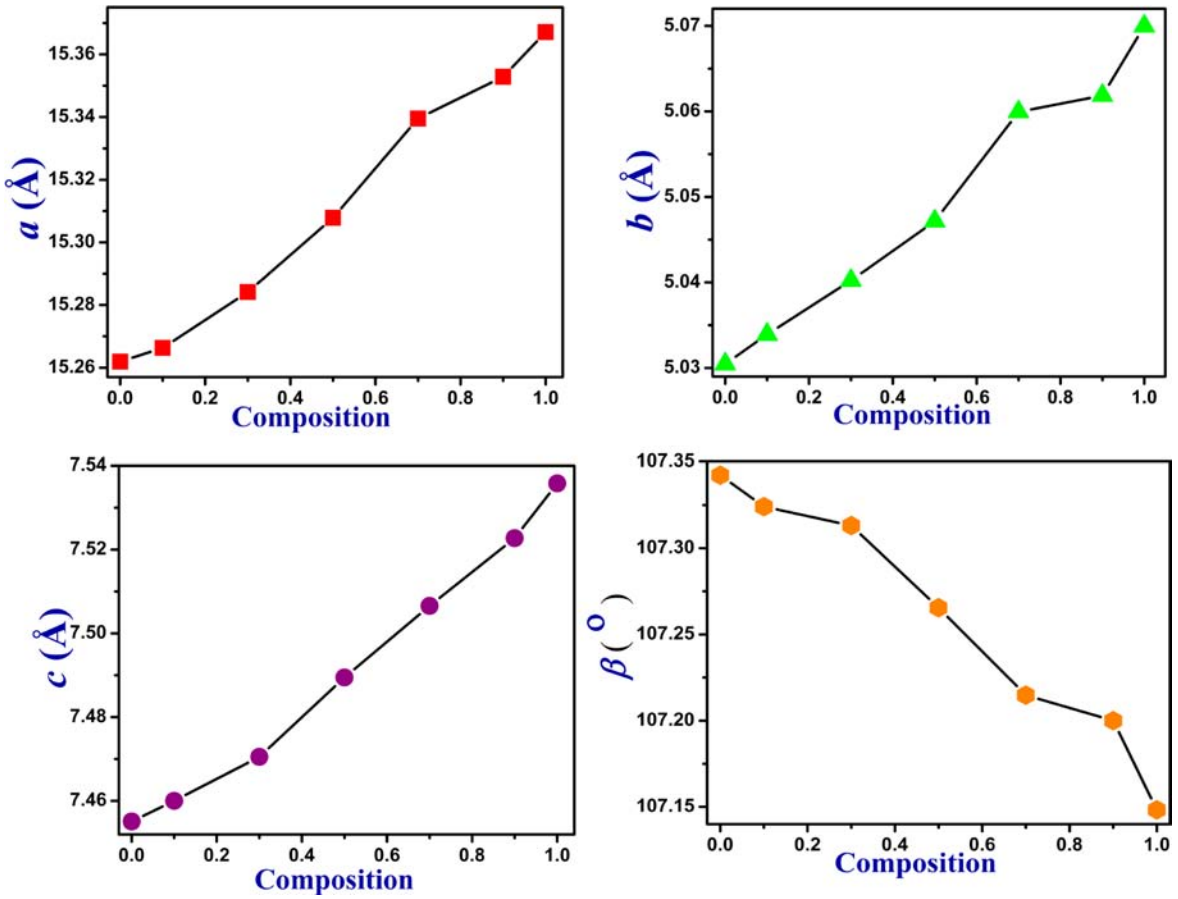

Figure 2. Plots of the changes in unit cell parameters with increasing Cu(I) content in the solid solution $Li_{1-x}Cu_xNb_3O_8$ ($0 \le x \le 1$).

stirring for several hours using a 1000 W Xe arc-lamp that is equipped with an IR water filter, >420 nm cutoff filter, and cooled using an external fan. The gaseous products were visually observed to rise to the top of the reaction vessel and collected in a horizontal glass tube that contained a movable liquid bubble. Gas products in the head space of the reaction vessel were manually injected into a gas chromatograph for identification.

Electronic Structure Calculations. Band-structure calculations were performed for several compositions of the $Li_{1-x}Cu_xNb_3O_8$ ($0 \le x \le 1$) solid solution with the use of the plane-wave density functional theory package CASTEP.[35] The solid solution compositions were modeled by doubling and/or tripling of each of the unit cell axes, followed by a reduction in space group symmetry to *P*1 (triclinic) to allow a random assignment of separate Cu and Li sites. The Perdew–Burke–Ernzerhof functional in the generalized gradient approximation and ultrasoft core potentials were employed in the calculations.[36a] The selection of equally distributed k-points within the Brillouin zone was automatically calculated according to the Monkhorst–Pack scheme.[36b]

RESULTS AND DISCUSSION

Characterization and Structure Description. Powder XRD data confirmed the phase purity across the entire range of composition of the $Li_{1-x}Cu_xNb_3O_8$ ($0 \le x \le 1$) solid solution, as shown in Figure 1. The crystal structures of MNb_3O_8 (M = Li, Cu) are previously reported to be monoclinic and isostructural.[37,38] Previously, a profile-only fitting of powder X-ray data for $CuNb_3O_8$ gave lattice constants and a unit cell volume about 0.6%–0.9% larger for M = Cu. The lattice constants across the entire $Li_{1-x}Cu_xNb_3O_8$ ($0 \le x \le 1$) solid solution approximately follow Vegard's law, shown in Figure 2, and reflect the unit-cell expansion from x = 0 to 1. The ionic radii of Cu^+ and Li^+ are 0.77 and 0.76 Å, respectively, in octahedral coordination environments. Thus, the increase in unit cell volume with increasing Cu(I) content is in accordance with the trend in the ionic radii. The increases in *a*, *b*, and *c* cell parameters are ~0.105, 0.040, and 0.081 Å, respectively, when going from $LiNb_3O_8$ to $CuNb_3O_8$.

Rietveld refinements of the powder XRD data were carried out for three compositions, x = 0.09, 0.50, and 0.70, with selected crystal refinement data and plots provided in Figure 3 and Tables 1 and 2. The compound crystallizes in the monoclinic crystal system (space group $P2_1/a$) with a = 15.262 Å, b = 5.033 Å, c = 7.457 Å, and β = 107.34°. Selected interatomic distances and bond valence sums around each metal site are listed in Table 3 for the x = 0.09 composition. Each composition was found to crystallize in the monoclinic crystal system (space group $P2_1/a$). Allowing the Cu and Li atoms to mix onto the same site yielded refined compositions that were all within ~5–10% of the loaded Cu:Li molar ratio in the solid-state reaction. The final R_p factors were 6.2%, 5.8%, and 5.32%, for the compositions x = 0.09, 0.50, and 0.70, respectively. Further refinement details can be found in the Supporting Information. The crystal structures of MNb_3O_8 (M = Cu, Li) have previously been described as a superstructure based on the orthorhombic PbO_2-structure type. Shown in Figures 4 and 5, the structure consists of zigzag chains of distorted NbO_6 and $(Li/Cu)O_6$ octahedra along the *b* axis. The Nb(2) and Nb(3) sites are contained in the former, whereas the Nb(1) and the Cu/Li atoms are contained in the latter. Within the chains of NbO_6 octahedra, the Nb(2)/Nb(3)–O bond distances can be divided into shorter bond distances of

dx.doi.org/10.1021/ic302649s | Inorg. Chem. 2013, 52, 4443–4450

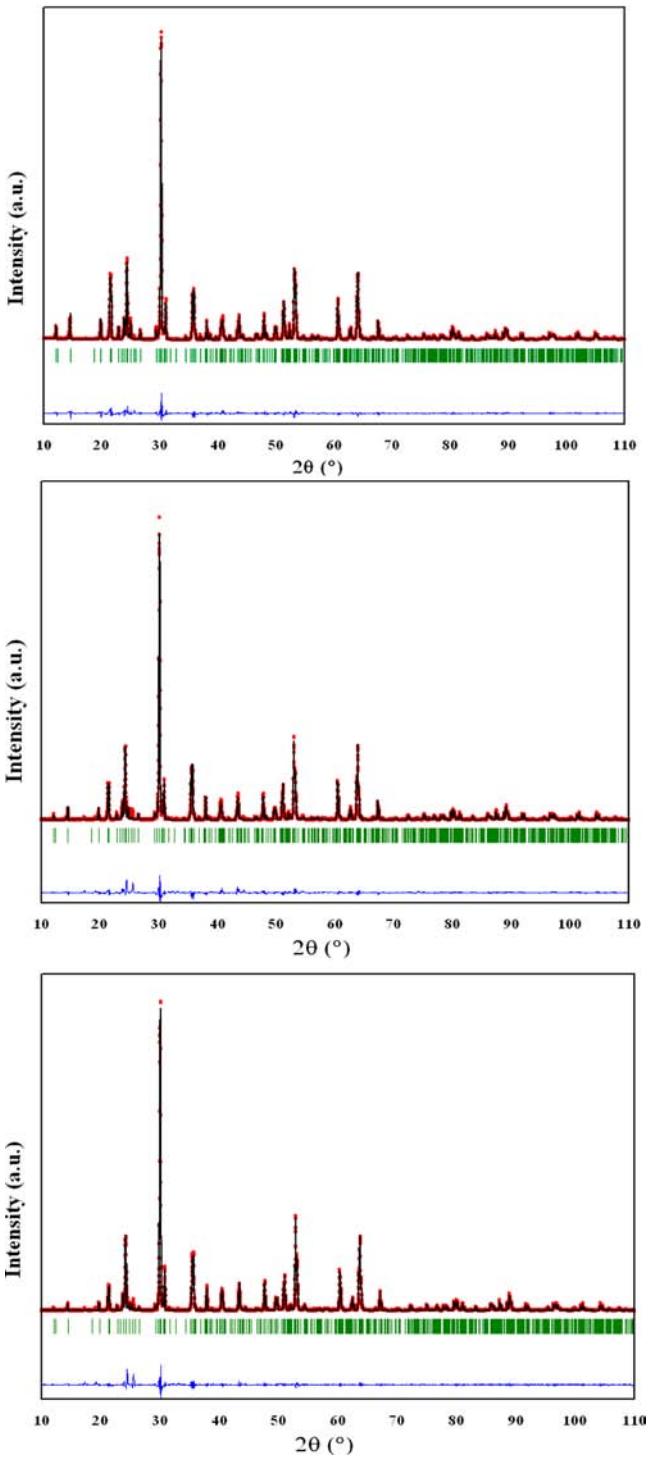

Figure 3. Rietveld refinement results for $Li_{0.91}Cu_{0.09}Nb_3O_8$(upper), $Li_{0.50}Cu_{0.50}Nb_3O_8$(middle), and $Li_{0.30}Cu_{0.70}Nb_3O_8$ (lower). The observed profile is indicated by circles, and the calculated profile is indicated by the solid line. Bragg peak positions are indicated by vertical tics, and the difference is shown at the bottom.

1.80−2.12 Å, and longer distances of 2.23−2.37 Å [Nb(2)−O(3), Nb(3)−O(8)]. The local interatomic distances around each metal are within the same ranges as previously reported.

Optical Absorption and Photocatalytic Properties. Transition-metal oxides combining Nb(V)/Ta(V) and Cu(I) in their structures have been shown to yield visible-light band gap sizes due to a metal-to-metal transition between the filled d^{10} and empty d^0-based crystal orbitals, respectively. Previous examples include $CuNbO_3$, $CuNb_3O_8$, $Cu_5Ta_{11}O_{30}$, and $Cu_3Ta_7O_{19}$.[21−24] In the present investigation, the formation of a $Li_{1-x}Cu_xNb_3O_8$ ($0 \leq x \leq 1$) solid solution allows the measurement of the more continuous formation of the new valence band with increasing Cu(I) content. The optical band gap sizes of several members of the solid solution (x = 0, 0.01, 0.03, 0.05, 0.07, 0.09, 0.1, 0.3, 0.5, 0.7, 0.9, and 1.0) have been extracted from the corresponding Tauc plots for both the direct and the indirect band gap transitions, shown in Figure 6. The band gap sizes were calculated from the rise in the onset of absorption with the equation E_g (eV) = 1240/λ (nm) and are listed in Table 4. Tauc plots for each of the individual compositions are given in the Supporting Information.

With the exception of $LiNb_3O_8$, all of the solid-solution compositions exhibit an indirect band gap transition that is lower in energy than the direct band gap transition. Members of this solid solution with the larger Cu(I) concentration (x = 0.1−0.9), Figure 6c and d, show a dramatic red-shift from ∼3.89 eV (direct) for $LiNb_3O_8$ to ∼1.45 and ∼1.27 eV (direct and indirect) for $CuNb_3O_8$. Even at concentrations as low as 10% Cu(I), that is, x = 0.1, the new valence band is nearly fully formed, as shown by its band gap transitions of 1.39 and 1.75 eV (direct and indirect). At lower Cu(I) concentrations of x = 0.01−0.07, Figure 6a and b, a large and distinct preabsorption-edge peak emerges at ∼2.72 eV (∼455 nm). This peak corresponds to electronic transitions between isolated Cu $3d^{10}$ orbitals and the Nb-based conduction-band states, as described below. Thus, at low Cu(I) content, there remains the large absorption edge from pure $LiNb_3O_8$ that stays relatively constant, as well as that from the isolated Cu $3d^{10}$ orbitals. These two different electronic transitions correspond to the two listed band gap sizes in Table 5. The overall pattern reveals a rapid emergence of the $3d^{10}$ orbitals between x = 0.01−0.07, and after the full formation of the higher-energy valence band, a continuous and smaller gradual red-shifting of the absorption edges and band gap sizes from x = 0.09−1.0.

Electronic structure calculations were performed for several different compositions of $Li_{1-x}Cu_xNb_3O_8$ ($0 \leq x \leq 1$) solid solution, and which gave generally similar and consistent results with each other. As previously reported for $CuNb_3O_8$,[22] the lowest energy band gap transition is between the filled $3d^{10}$-based crystal orbitals on Cu(I) and the empty d^0-based crystal orbitals on Nb(V), as well as some small O 2p-orbital contributions in each. By contrast, in pure $LiNb_3O_8$ the valence band is instead comprised of the O 2p-based crystal orbitals. Shown in Figure 7 is an electron density contour plot (blue-colored) of the highest-energy valence band states for the x = 0.5 composition, that is, $Li_{0.5}Cu_{0.5}Nb_3O_8$. The Cu and Li sites in different chains of the structure have been randomly assigned as an alternating pattern of either 3 Li sites and 1 Cu site (upper and lower chain), or 1 Cu site and 3 Li sites (middle chain). In both types of chains, the valence-band electron density is shown to be delocalized entirely over the Cu(I) sites, which interact with each other through intervening O-2p/Nb-4d orbitals. The conduction band electron density in each case is entirely delocalized over the Nb(V) sites. This leads to the rapid formation of a valence band at even low Cu(I) concentrations in the solid solution.

Photocatalysis. Photocatalytic reactions via semiconductor powders in aqueous solutions proceed by the absorption of light and the excitation of electrons into the conduction band. The space-charge layer at the surface serves as a driving force

dx.doi.org/10.1021/ic302649s | Inorg. Chem. 2013, 52, 4443−4450

Table 1. Selected Refinement Parameters for Rietveld Refinements of Three Solid Solution Compositions: $Li_{0.91}Cu_{0.09}Nb_3O_8$, $Li_{0.5}Cu_{0.5}Nb_3O_8$, and $Li_{0.3}Cu_{0.7}Nb_3O_8$

reactant formula	$Li_{0.91}Cu_{0.09}Nb_3O_8$	$Li_{0.50}Cu_{0.50}Nb_3O_8$	$Li_{0.30}Cu_{0.70}Nb_3O_8$
refined formula	$Li_{0.867}Cu_{0.133}Nb_3O_8$	$Li_{0.535}Cu_{0.465}Nb_3O_8$	$Li_{0.38}Cu_{0.62}Nb_3O_8$
space group, Z	$P2_1/a$, 4	$P2_1/a$, 4	$P2_1/a$, 4
radiation	Cu $K\alpha_1$= 1.54051 Å	Cu $K\alpha_1$= 1.54051 Å	Cu $K\alpha_1$= 1.54051 Å
crystal system	monoclinic	monoclinic	monoclinic
a/Å	15.27073(3)	15.3138(2)	15.33006(3)
b/Å	5.03521(4)	5.0526(3)	5.059458(12)
c/Å	7.46174(2)	7.4926(3)	7.50438(2)
β/deg	107.322(2)	107.2561(3)	107.2250(5)
volume/Å^3	547.722 (8)	553.64(4)	555.981(3)
R_p, R_{wp}	0.0620, 0.0904	0.0580, 0.0823	0.0532, 0.0754
2θ (deg) range	5−110	5−110	5−110
no. of unique data	5834	5834	5834

Table 2. Refined Atomic Coordinates, Isotropic Displacement Parameters (Å^2), and Site Occupancies for $Li_{0.91}Cu_{0.09}Nb_3O_8$

atomic and Wyckoff position	x	y	z	U_{eq} (Å^2)	occupancy
Li(1)/Cu(1) (4e)	0.419(3)	0.276(15)	0.272(7)	0.023(18)	0.867/0.113
Nb(1) (4e)	0.1681(4)	0.270(2)	0.0068(7)	0.0204(19)	1.0
Nb(2) (4e)	0.0744(4)	0.755(2)	0.2490(9)	0.0251(15)	1.0
Nb(3) (4e)	0.1642(4)	0.256(2)	0.5156(7)	0.0201(18)	1.0
O(1) (4e)	0.280(3)	0.433(8)	0.080(6)	0.012(14)	1.0
O(2) (4e)	0.0.149(3)	0.395(7)	0.736(7)	0.014(14)	1.0
O(3) (4e)	0.292(3)	0.073(8)	0.591(6)	0.012(14)	1.0
O(4) (4e)	−0.042(3)	0.889(8)	0.149(5)	0.003(13)	1.0
O(5) (4e)	0.093(3)	−0.049(8)	0.511(6)	0.015(15)	1.0
O(6) (4e)	0.046(3)	0.424(8)	0.355(6)	0.017(14)	1.0
O(7) (4e)	0.099(3)	0.575(9)	0.024(7)	0.033(18)	1.0
O(8) (4e)	0.154(3)	0.085(8)	0.224(7)	0.032(17)	1.0

Table 3. Selected Interatomic Distances and Bond Valence Sums for $Li_{0.91}Cu_{0.09}Nb_3O_8$

bond length type		distance (Å)	bond length type		distance (Å)
Nb(1)	−O(1)	1.82(4)	Nb(2)	−O(3)	2.23(4)
	−O(1)	2.06(4)		−O(4)	1.84(4)
	−O(2)	2.05(5)		−O(5)	2.13(5)
	−O(4)	2.09(4)		−O(6)	1.95(5)
	−O(7)	1.89(5)		−O(7)	2.04(5)
	−O(8)	1.94(5)		−O(8)	2.10(5)
bond valence sum		4.7(5)	bond valence sum		4.7(4)
Nb(3)	−O(2)	1.86(5)	Li(1)/Cu(1)	−O(1)	2.33(6)
	−O(3)	2.08(4)		−O(2)	2.18(8)
	−O(3)	1.99(5)		−O(4)	2.09(8)
	−O(5)	1.87(4)		−O(5)	1.90(8)
	−O(6)	2.02(4)		−O(6)	2.11(7)
	−O(8)	2.30(5)		−O(7)	2.37(7)
bond valence sum		4.9(5)	bond valence sum		0.93(9)/ 1.03(11)

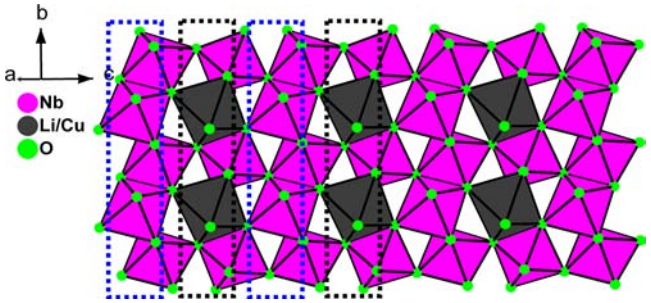

Figure 4. Polyhedral representation of the structure of $Li_{1-x}Cu_xNb_3O_8$. The blue and the black slabs represent zigzag strings of either only NbO_6 octahedra or alternating $(Cu/Li)O_6$ and NbO_6 octahedra, respectively.

for the separation of the excited electron−hole pairs, which can be used to drive the reduction or oxidation of water by the electrons and holes, respectively. Overall water splitting, that is, both reduction and oxidation at the same time and surfaces, is both difficult and unnecessary if the semiconductor is used as a p- or n-type photoelectrode and connected through an external circuit to a counter electrode. In the form of a suspended-powder photocatalyst, a sacrificial reagent is typically used to scavenge the excited holes to investigate just the reduction half-reaction of water splitting. Several members of the $Li_{1-x}Cu_xNb_3O_8$ ($0 \le x \le 1$) solid solution were loaded with a 1% Pt surface cocatalyst, suspended in an aqueous solution of 20% methanol, and then measured under visible-light irradiation for their photocatalytic activity for the reduction of water to hydrogen. The methanol functions as a hole scavenger, thereby generating both H_2 as the reduction product as well as CO_2 rather than O_2 as the oxidation product.[39] A control experiment with an aqueous solution of 20% methanol solution did not produce any hydrogen under UV irradiation without the solid-solution catalyst. Powder XRD data were taken both before and after the photocatalytic measurement to confirm the crystallinity and purity of the product was maintained.

The photocatalytic activities for the x = 0, 0.03, 0.07, 0.09, 0.3, 0.5, 0.7, and 1.0 members of the $Li_{1-x}Cu_xNb_3O_8$ solid

dx.doi.org/10.1021/ic302649s | Inorg. Chem. 2013, 52, 4443−4450

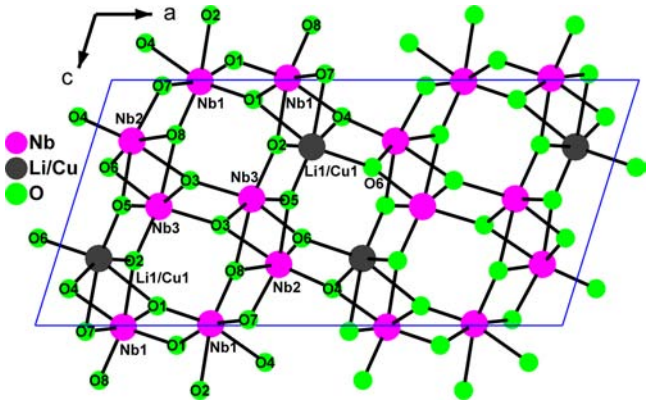

Figure 5. Asymmetric unit view of a single layer through the unit cell of $Li_{1-x}Cu_xNb_3O_8$.

solution are listed in Table 5. The pure $LiNb_3O_8$ exhibited the highest photocatalytic activity under only UV-irradiation, producing 83.87 μmol of hydrogen (50 mg of photocatalyst) in 1 h, and that continued at a steady rate. This result is in agreement with previously reported results on $LiNbO_3$ and $LiNb_3O_8$ photocatalysts under similar conditions.[40] When using visible-light irradiation, $LiNb_3O_8$ does not produce any hydrogen due to its large band gap size and inability to absorb visible light. However, the substitution of Cu(I) into the

Table 4. Measured Direct and Indirect Band Gap Sizes from Tauc Plots of Several Members of the $Li_{1-x}Cu_xNb_3O_8$ ($0 \le x \le 1$) Solid Solution

		direct band gap (eV) absorption edges	
chemical formula	indirect band gap (eV) absorption edges	no. 1	no. 2
$LiNb_3O_8$			3.891
$Li_{0.99}Cu_{0.01}Nb_3O_8$	1.501	1.909	3.830
$Li_{0.97}Cu_{0.03}Nb_3O_8$	1.413	1.883	3.828
$Li_{0.95}Cu_{0.05}Nb_3O_8$	1.396	1.864	3.823
$Li_{0.93}Cu_{0.07}Nb_3O_8$	1.391	1.779	3.797
$Li_{0.91}Cu_{0.09}Nb_3O_8$	1.390	1.752	
$Li_{0.9}Cu_{0.1}Nb_3O_8$	1.386	1.750	
$Li_{0.7}Cu_{0.3}Nb_3O_8$	1.333	1.608	
$Li_{0.5}Cu_{0.5}Nb_3O_8$	1.322	1.539	
$Li_{0.3}Cu_{0.7}Nb_3O_8$	1.295	1.495	
$Li_{0.1}Cu_{0.9}Nb_3O_8$	1.283	1.454	
$CuNb_3O_8$	1.267	1.445	

$Li_{1-x}Cu_xNb_3O_8$ solid solution results in from ~7 to 18 μmol of hydrogen in 1 h under visible-light irradiation. The rate peaks at approximately the midpoint of the solid solution composition, that is, at $x = 0.5$, as well as for the pure $CuNb_3O_8$. The total number of NbO_6 surface sites (T_{surf} (mol Nb)), and thus the

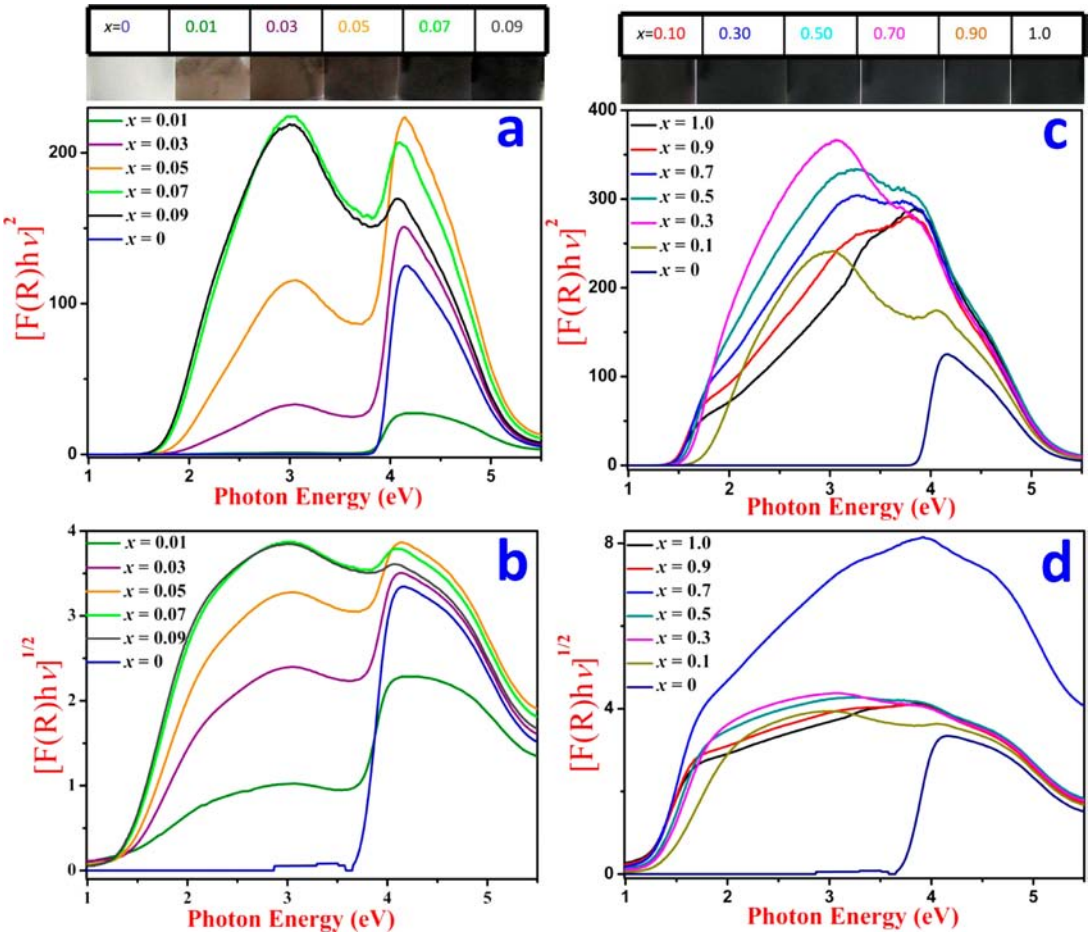

Figure 6. Tauc plots of $[F(R)h\nu]^n$ versus $[h\nu]$ ($n = 2$ and 1/2 for direct (a and c) and indirect (b and d) band gap transitions, respectively) for the UV–vis diffuse reflectance spectra of members of the $Li_{1-x}Cu_xNb_3O_8$ ($0 \le x \le 1$) solid solution. The color of the samples changed from pristine white ($x = 0$) to brown ($x = 0.03$–0.07) to black ($x = 0.09$–1.0) with the increase in Cu(I) content of the solid solution.

dx.doi.org/10.1021/ic302649s | Inorg. Chem. 2013, 52, 4443–4450

Table 5. Measured Photocatalytic Activities of Each of the Solid Solutions for Water Reduction to Hydrogen under Visible-Light Irradiation[a]

catalyst composition	color	cocatalyst loading and wavelength (nm)		total H_2 (μmol) after 1 h	total turnover per NbO_6 surface site
$LiNb_3O_8$	white	1% Pt	>420	0	
$Li_{0.97}Cu_{0.03}Nb_3O_8$	brown	1% Pt	>420	6.66	15.86
$Li_{0.93}Cu_{0.07}Nb_3O_8$	dark brown	1% Pt	>420	7.55	17.98
$Li_{0.91}Cu_{0.09}Nb_3O_8$	black	1% Pt	>420	9.54	22.71
$Li_{0.70}Cu_{0.30}Nb_3O_8$	black	1% Pt	>420	11.73	27.93
$Li_{0.50}Cu_{0.50}Nb_3O_8$	black	1% Pt	>420	18.29	43.55
$Li_{0.30}Cu_{0.70}Nb_3O_8$	black	1% Pt	>420	7.95	18.93
$CuNb_3O_8$	black	1% Pt	>420	12.33	29.34

[a]Samples were prepared by solid-state reactions in evacuated silica ampules at 750 °C for 2 days.

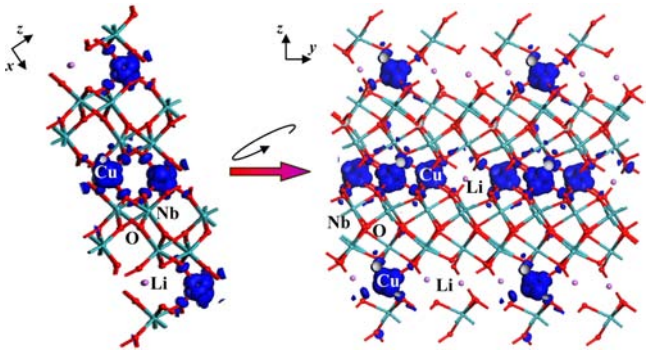

Figure 7. Electron density contour plots of the highest-energy region of the valence band (blue electron density) for the $x = 0.5$ member of the $Li_{1-x}Cu_xNb_3O_8$ solid solution. The structural picture on the left is oriented down the *y*-axis, while that on the right is oriented down the *x*-axis.

turnover number and frequency, can be estimated from the total measured surface area of the sample (a_{surf} (g/m^2)), the weight of the sample (W (g)), and the average density of the surface sites (d_{surf} (mol Nb/m^2)) from each of the main types of crystal faces: $T_{surf} = a_{surf} \times W \times d_{surf}$. Using the measured values for a_{surf} (0.42 m^2/g) and W (0.1 g), and the calculated d_{surf} (1.0×10^{-5} mol Nb/m^2), gives a total number of NbO_6 surface sites of $T_{surf} = 0.42$ μmol Nb. Thus, after the first hour, a total turnover of between 16 and 44 is observed, confirming the hydrogen production reaction is photocatalytic in nature. The turnover number peaks at the same compositions where the photocatalysis rates are the highest. The rate of hydrogen production starts to significantly slow after an hour or two. Further investigations are also necessary to describe the full influence of the amount of photocatalyst, cocatalyst loading, pH, and method of synthesis, for example, on the photocatalytic activity in a follow-up study.

CONCLUSIONS

A new solid solution $Li_{1-x}Cu_xNb_3O_8$ ($0 \le x \le 1$) has been prepared by solid-state techniques with a range of compositions between $CuNb_3O_8$ and $LiNb_3O_8$. The optical band gap size across the solid solution exhibits a significant red-shift from ~3.89 eV (direct) to ~1.45 eV and ~1.27 eV (direct and indirect) with increasing Cu(I) content, consistent with the change in sample color from white to dark brown to black. Electronic structure calculations show the formation of a new Cu $3d^{10}$-based valence band that emerges higher in energy than the O 2p band. While the pure $LiNb_3O_8$ is a highly active UV-photocatalyst for water reduction, the $Li_{1-x}Cu_xNb_3O_8$ solid solution is shown to be photocatalytically active under visible-light irradiation for water reduction to hydrogen.

ASSOCIATED CONTENT

Supporting Information

Crystallographic information files obtained from the Rietveld refinement, a plot of change in unit cell volume with increasing Cu(I) content in the solid solution $Li_{1-x}Cu_xNb_3O_8$ ($0 \le x \le 1$), measured UV−vis diffuse reflectance spectra for $Li_{1-x}Cu_xNb_3O_8$ ($0 \le x \le 1$), and direct and indirect band gap calculation for the various members of the solid solution. This material is available free of charge via the Internet at http://pubs.acs.org.

AUTHOR INFORMATION

Corresponding Author

*Phone: 919-551-3616. E-mail: paul_maggard@ncsu.edu.

Notes

The authors declare no competing financial interest.

ACKNOWLEDGMENTS

We acknowledge support of this research from the National Science Foundation (DMR-0644833), from the Research Corporation for Science Advancement (P.M. is a Scialog Awardee), and also assistance with the collection of high-resolution PXRD data (H.-C. zur Loye).

REFERENCES

(1) Osterloh, F. E. *Chem. Mater.* **2008**, *20*, 35−54.
(2) Abe, R. *J. Photochem. Photobiol., C* **2010**, *11*, 179−209.
(3) Fujishima, A.; Honda, K. *Nature* **1972**, *238*, 37.
(4) Ni, M.; Leung, M. K. H.; Leung, D. Y. C.; Sumathy, K. *Renewable Sustainable Energy Rev.* **2007**, *11*, 401−425.
(5) Joshi, U. A.; Palasyuk, A.; Arney, D.; Maggard, P. A. *J. Phys. Chem. Lett.* **2010**, *1*, 2719−2726.
(6) Chen, X.; Shen, S.; Guo, L.; Mao, S. S. *Chem. Rev.* **2010**, *110*, 6503−6570.
(7) Walter, M. G.; Warren, E. L.; McKone, J. R.; Boettcher, S. W.; Mi, Q.; Santori, E. A.; Lewis, N. S. *Chem. Rev.* **2010**, *110*, 6446−6473.
(8) Asahi, R.; Morikawa, T.; Ohwaki, T.; Aoki, K.; Taga, Y. *Science* **2001**, *293*, 269−271.
(9) Khan, S. U. M.; Al-Shahry, M.; Ingler, W. B. *Science* **2002**, *297*, 2243−2245.
(10) Sakthivel, S.; Kisch, H. *Angew. Chem., Int. Ed.* **2003**, *42*, 4908−4911.
(11) Tang, J.; Zou, Z.; Ye, J. *Angew. Chem., Int. Ed.* **2004**, *43*, 4463−4466.
(12) Kim, H. G.; Hwang, D. W.; Lee, J. S. *J. Am. Chem. Soc.* **2004**, *126*, 8912−8913.
(13) Fu, H. B.; Pan, C. S.; Yao, W. Q.; Zhu, Y. F. *J. Phys. Chem. B* **2005**, *109*, 22432−22439.
(14) Fu, H. B.; Zhang, L. W.; Yao, W. Q.; Zhu, Y. F. *Appl. Catal., B* **2006**, *66*, 100−110.
(15) Tang, J. W.; Zou, Z. G.; Ye, J. H. *Chem. Mater.* **2004**, *16*, 1644−1649.

(16) Kato, H.; Kobayashi, H.; Kudo, A. *J. Phys. Chem. B* **2002**, *106*, 12441−12447.
(17) Maruyama, Y.; Irie, H.; Hashimoto, K. *J. Phys. Chem. B* **2006**, *110*, 23274−23278.
(18) Kudo, A.; Miseki, Y. *Chem. Soc. Rev.* **2009**, *38*, 253−278.
(19) Arney, D.; Watkins, T.; Maggard, P. A. *J. Am. Ceram. Soc.* **2011**, *94*, 1483−1489.
(20) Arney, D.; Hardy, C.; Greve, B.; Maggard, P. A. *J. Photochem. Photobiol., A* **2010**, *214*, 54−60.
(21) Joshi, U. A.; Palasyuk, A.; Maggard, P. A. *J. Phys. Chem. C* **2011**, *115*, 13534−13539.
(22) Joshi, U. A.; Maggard, P. A. *J. Phys., Lett.* **2012**, *3*, 1577−1581.
(23) Palasyuk, O.; Palasyuk, A.; Maggard, P. A. *J. Solid State Chem.* **2010**, *183*, 814−822.
(24) Fuoco, L.; Joshi, U. A.; Maggard, P. A. *J. Phys. Chem. C* **2012**, *116*, 10490−10497.
(25) Palasyuk, O.; Palasyuk, A.; Maggard, P. A. *Inorg. Chem.* **2010**, *49*, 10571−10578.
(26) Dusek, M.; Petricek, V.; Wunschel, M.; Dinnebier, R. E.; van Smaalen, S. *J. Appl. Crystallogr.* **2001**, *34*, 398−404.
(27) Morales, A. E.; Mora, E. S.; Pal, U. *Rev. Mex. Fis. S* **2007**, *53*, 18−22.
(28) Kubelka, P.; Munk, F. *Z. Tech. Phys.* **1931**, *12*, 593.
(29) Tauc, J.; Grigorovici, R.; Vancu, A. *Phys. Status Solidi* **1966**, *15*, 627.
(30) Kato, H.; Asakura, K.; Kudo, A. *J. Am. Chem. Soc.* **2003**, *125*, 3082−3089.
(31) Matsuoka, M.; Kitano, M.; Takeuchi, M.; Tsujimaru, K.; Anpo, M.; Thomas, J. M. *Catal. Today* **2007**, *122*, 51−61.
(32) Borgarello, E.; Kiwi, J.; Pelizzetti, E.; Visca, M.; Grätzel, M. *Nature* **1981**, *289*, 158−160.
(33) Linsebigler, A. L.; Lu, G.; Yates, J. T. *Chem. Rev.* **1995**, *95*, 735−738.
(34) Nakamatsu, H.; Kawai, T.; Koreeda, A.; Kawai, S. *J. Chem. Soc., Faraday Trans.* **1986**, *82*, 527−531.
(35) Clark, S. J.; Segall, M. D.; Pickard, C. J.; Hasnip, P. J.; Probert, M. J.; Refson, K.; Payne, M. C. *Z. Kristallogr.* **2005**, *220*, 567.
(36) (a) Payne, M. C.; Teter, M. P.; Allan, D. C.; Arias, T. A.; Joannopoulos, J. D. *Rev. Mod. Phys.* **1992**, *64*, 1045. (b) Monkhorst, H. J.; Pack, J. D. *Phys. Rev. B* **1976**, *13*, 5188.
(37) Lundberg, M. *Acta Chem. Scand.* **1971**, *25*, 3337−3346.
(38) Marinder, B.-O.; Werner, P.-E.; Wahlström, E.; Malmros, G. *Acta Chem. Scand.* **1980**, *34*, 51−56.
(39) Choi, H.-J.; Kang, M. *Int. J. Hydrogen Energy* **2007**, *32*, 3841−3848.
(40) Zielińska, B.; Borowiak-Palen, E.; Kalenzuk, R. J. *J. Phys. Chem. Solids* **2008**, *69*, 236−242.